MATERIALS SCIENCE

Mechanism and performance relevance of nanomorphogenesis in polyamide films revealed by quantitative 3D imaging and machine learning

Hyosung An[1,2], John W. Smith[1], Bingqiang Ji[3], Stephen Cotty[4], Shan Zhou[1], Lehan Yao[1], Falon C. Kalutantirige[5], Wenxiang Chen[1,2], Zihao Ou[1], Xiao Su[4], Jie Feng[2,3], Qian Chen[1,2,4,5,6]*

Biological morphogenesis has inspired many efficient strategies to diversify material structure and functionality using a fixed set of components. However, implementation of morphogenesis concepts to design soft nanomaterials is underexplored. Here, we study nanomorphogenesis in the form of the three-dimensional (3D) crumpling of polyamide membranes used for commercial molecular separation, through an unprecedented integration of electron tomography, reaction-diffusion theory, machine learning (ML), and liquid-phase atomic force microscopy. 3D tomograms show that the spatial arrangement of crumples scales with monomer concentrations in a form quantitatively consistent with a Turing instability. Membrane microenvironments quantified from the nanomorphologies of crumples are combined with the Spiegler-Kedem model to accurately predict methanol permeance. ML classifies vastly heterogeneous crumples into just four morphology groups, exhibiting distinct mechanical properties. Our work forges quantitative links between synthesis and performance in polymer thin films, which can be applicable to diverse soft nanomaterials.

INTRODUCTION

Morphogenesis—the emergence of structure—occurs across length scales and by diverse physical and chemical mechanisms in biological systems. Examples include the deposition of diatom frustules (*1*), differential growth during embryonic development (*2*), and the self-assembly of the cytoskeleton (*3*). A key utility of these approaches lies in the ability to generate diverse morphological phenotypes—and therefore functions—from a fixed set of components. Biological morphogenesis has inspired strategies to pattern synthetic crystalline "biomorphs" (*4*, *5*), hydrogels (*6*), and composites (*7*, *8*) at or above the micrometer-scale. However, morphogenesis at the nanoscale, especially in amorphous soft materials, is not well understood. On the one hand, morphology quantification is challenging for these systems, because conventional ensemble structural characterization methods such as spectroscopy (*9*) and quartz crystal microbalance measurements (*10*) are not sufficient to characterize the three-dimensional (3D), nanoscale, and heterogeneous features they can exhibit. Recent work, including our own (*11*), successfully used scanning/transmission electron microscopy (S/TEM) tomography to reveal the complex inner and outer nanostructure of polymer membranes (*12–14*) and self-assembled block copolymer architectures (*15*). However, these 3D features have not yet been quantitatively related to synthesis conditions or local material properties. On the other hand, there are many theoretical models for morphogenesis—for example, based on differential growth, which is a pathway to establish macroscopic structure in plants (*16*) or the digestive system (*17*)—but these tend not to describe complexities that emerge when chemical reactions are involved. In general, quantitative

chemical models concerning molecular reactions far from equilibrium for the development of nanoscale structural features are lacking, further underscoring a need for experimental quantification of soft nanostructures for comparison.

Here, we developed an understanding of nanomorphogenesis in our model system of polyamide membranes, along with its effect on their permeance and mechanical heterogeneity, by coupling quantitative 3D imaging, machine learning (ML), and theoretical modeling. Polyamide membranes are the active layer in most thin-film composites used for energy-efficient molecular separations (*18*, *19*). These membranes are synthesized via interfacial polymerization, which produces films that are macroscopically flat but characterized by heterogeneous crumples containing inner voids at the nanoscale (*12*, *19*). Crumples are complex and 3D and are believed to play important roles in membrane performance (*14*, *20*, *21*). Hence, an understanding of their nanomorphogenesis is required as a quantitative link between synthesis conditions and performance metrics, such as separation efficiency and mechanical robustness. We used electron tomography with nanometer resolution to reconstruct the 3D morphology of a series of polyamide membranes synthesized with a range of monomer concentrations. We found pores beneath each crumple though not spanning across the membrane. The characteristic spatial wavelength of these pores follows a power law dependence on the monomer concentrations, a quantitative trend expected from a process described by Turing theory (*22*) and suggesting the involvement of a reaction-diffusion instability in crumple formation. Then, we identified an array of quantitative morphological parameters to describe the irregular 3D nanostructure of the crumples. The true membrane surface area and local thickness measured in this way were used as input to predict the permeance of each membrane using the Spiegler-Kedem model, which showed exceptional agreement with the experimental measurements. Morphological parameters were also used as input for unsupervised ML classification with a Gaussian mixture model (GMM), which allowed us to classify 151 crumples into just four types: domes,

[1]Department of Materials Science and Engineering, University of Illinois, Urbana, IL, USA. [2]Materials Research Laboratory, University of Illinois, Urbana, IL, USA. [3]Department of Mechanical Science and Engineering, University of Illinois, Urbana, IL, USA. [4]Department of Chemical and Biomolecular Engineering, University of Illinois, Urbana, IL, USA. [5]Department of Chemistry, University of Illinois, Urbana, IL, USA. [6]Beckman Institute for Advanced Science and Technology, University of Illinois, Urbana, IL, USA.
*Corresponding author. Email: qchen20@illinois.edu

dimples, pancakes, and clusters, regardless of synthesis conditions. These morphology groups have distinct local Young's moduli, resolved with nanometer resolution using liquid-phase atomic force microscopy (AFM). In short, we quantify cross-talk between synthesis conditions, 3D nanomorphology, and performance properties in polyamide membranes. These concepts may inspire strategies to expand the functionality of soft nanomaterials in general—polymers, vesicles, microgels, etc.—through morphogenesis and engineer their 3D nanomorphology during chemical reactions, folding, phase separation, or drying.

RESULTS
Variations in monomer concentration produce diverse membrane nanostructures
We used low-dose rate (4 to 7 e^- $Å^{-2}$ s^{-1}) electron tomography with no staining (11) to minimize beam-induced alteration and reconstruct the 3D nanostructure (with a final voxel size of 6.8 Å) of polyamide membranes synthesized with a range of monomer concentrations and a fixed reaction time (movie S1). Their synthesis by interfacial polymerization involves an aqueous phase containing an amine monomer [m-phenylenediamine (MPD) here] and an organic phase containing an acyl chloride monomer [here, trimesoyl chloride (TMC) in hexane] (Fig. 1A and figs. S1 and S2). Upon contact of the two phases, MPD can diffuse into hexane more readily than TMC into water, so polymerization occurs mostly in hexane near the water–hexane interface (23, 24). Interfacial polymerization eventually self-terminates because diffusion is blocked by the grown polymer film (25). The polymerization reaction is rapid and highly exothermic (24, 26). For this reason, conflicting hypotheses involving local heating (27, 28), rapid diffusion of amines into the organic phase after formation of an incipient layer (21), and generation of nano-bubbles (28) have been proposed as possible mechanisms for crumple formation. However, the dominant contributor to morphogenesis has up to now been unclear, especially due to a lack of quantitative nanostructure analysis across different synthesis conditions. As shown in the reconstructed 3D tomograms (Fig. 1B and movie S2), variations in the monomer concentration alone (c_{MPD}, 1 to 5 w/v%; c_{TMC}, 0.05 to 1 w/v%) lead to distinct nanostructures, ranging from crumples of different sizes and areal number densities (Materials and Methods, fig. S1, and table S1) to completely interconnected networks [Fig. 1B, bottom right, polyamide (5, 0.05)]. Samples obtained at a reaction time longer than 1 min do not show a difference in morphology (fig. S1B).

Electron tomography differentiates inner voids and pores from the polymer volume of the membrane, and these features are present in all 151 crumples that we analyzed for the membranes synthesized at different conditions (fig. S3). Figure 1 (C and D) shows cross-sectional views of two types of crumples. The first we call solo crumples, consisting of one nodule and generally one bottom pore (Fig. 1C and fig. S4, 129 of 135 solo crumples have one bottom pore; $N_P = 1.1 \pm 0.4$ for number of pores per crumple, Fig. 1E). The second we refer to as cluster crumples, composed of merged nodules with multiple pores (Fig. 1D and fig. S5, from 16 cluster crumples; $N_P = 9.2 \pm 4.8$, Fig. 1E). The collocation of the pore(s) and a nodule suggests that pore formation and nodule protrusion accompany one another (fig. S6A). Here, the pores are not open ones but can be seen effectively as a concave region formed because of the bulging of a continuous membrane. Pores have been noted in previous SEM studies of the back surface of polyamide membrane and also in our

samples (fig. S6), but have not been resolved simultaneously with the top nodule on the front side to confirm their collocation (29). We also confirmed that the synthesized membranes are not defective by performing permeability tests showing no permeability against water (fig. S7).

Pore distributions quantitatively link film morphogenesis to a reaction-diffusion instability
The lateral spatial distribution of pores strongly depends on the monomer concentrations, and quantitative characterization of this relationship provides evidence for a hypothesis that crumple protrusion is associated with a Turing reaction-diffusion instability. In particular, Turing's theory (22) predicts that when two species with sufficiently different diffusivities react and diffuse with each other, spatial patterns will be generated with a wavelength following a power law dependence on the monomer concentrations and diffusivities (30). Previous studies have suggested a connection between film morphologies and a Turing-like reaction-diffusion process (24, 31), but their lack of structural characterization did not allow for quantitative validation. Our comprehensive reconstructions across synthesis conditions allow us to test the Turing hypothesis quantitatively. In particular, we analyzed the spatial distribution of more than 2000 pores in the membranes that we studied using Delaunay triangulation (Materials and Methods, Fig. 2, A to D, and figs. S8 to S10), from which a characteristic wavelength λ (i.e., averaged distance d between neighboring pores, see fig. S10) can be measured (table S2). Our data are well described by

$$\lambda \sim \delta^{1/2} \rho^{1/2} m_{MPD}^{1/2} D_{TMC}^{1/4} c_{MPD}^{-1/2} c_{TMC}^{-1/4} \qquad (1)$$

where δ is the membrane thickness (table S1), ρ is the polymer density assuming a linear relationship between polymer density and degree of cross-linking (19, 32), m_{MPD} is the mass fraction of MPD in membranes (Materials and Methods and table S3), and $D_{TMC} \approx 10^{-9}$ m^2/s (31, 33) is the diffusion coefficient of TMC in hexane. Equation 1 is the mathematical form expected from a Turing reaction-diffusion process (for a complete derivation, see Materials and Methods). As shown in Fig. 2E, our experimentally measured λ for the membranes relates to monomer concentrations following Eq. 1, validating that the main trend behind of the pore and crumple distancing could be captured by a reaction-diffusion instability. The corresponding interfacial polymerization time τ, given an MPD diffusion coefficient (31) D_{MPD}, is estimated by

$$\tau = \lambda^2 (2\pi)^{-1} D_{MPD}^{-1/2} D_{TMC}^{-1/2} \qquad (2)$$

to fall in the range of 1 to 10 μs, which is consistent with the reaction time reported in the literature (23).

We also provide evidence against earlier hypotheses that membrane crumpling is dominated by hydrodynamic phenomena. For example, spatial patterns can also develop in thin liquid films because of Rayleigh-Bénard or Bénard-Marangoni instabilities (34). Onset of these instabilities requires that the critical Rayleigh number (Ra, comparing buoyancy-driven convective thermal transport to diffusive thermal transport) or the critical Marangoni number (Ma, comparing interfacial tension gradient-driven transport to diffusive thermal transport) exceeds 660 to 1700 or 50 to 80, respectively (35). In our system, $Ra \approx 10^{-12}$ and $Ma \approx 10^{-1}$ (Materials and Methods), which are far too small to induce either instability. Other
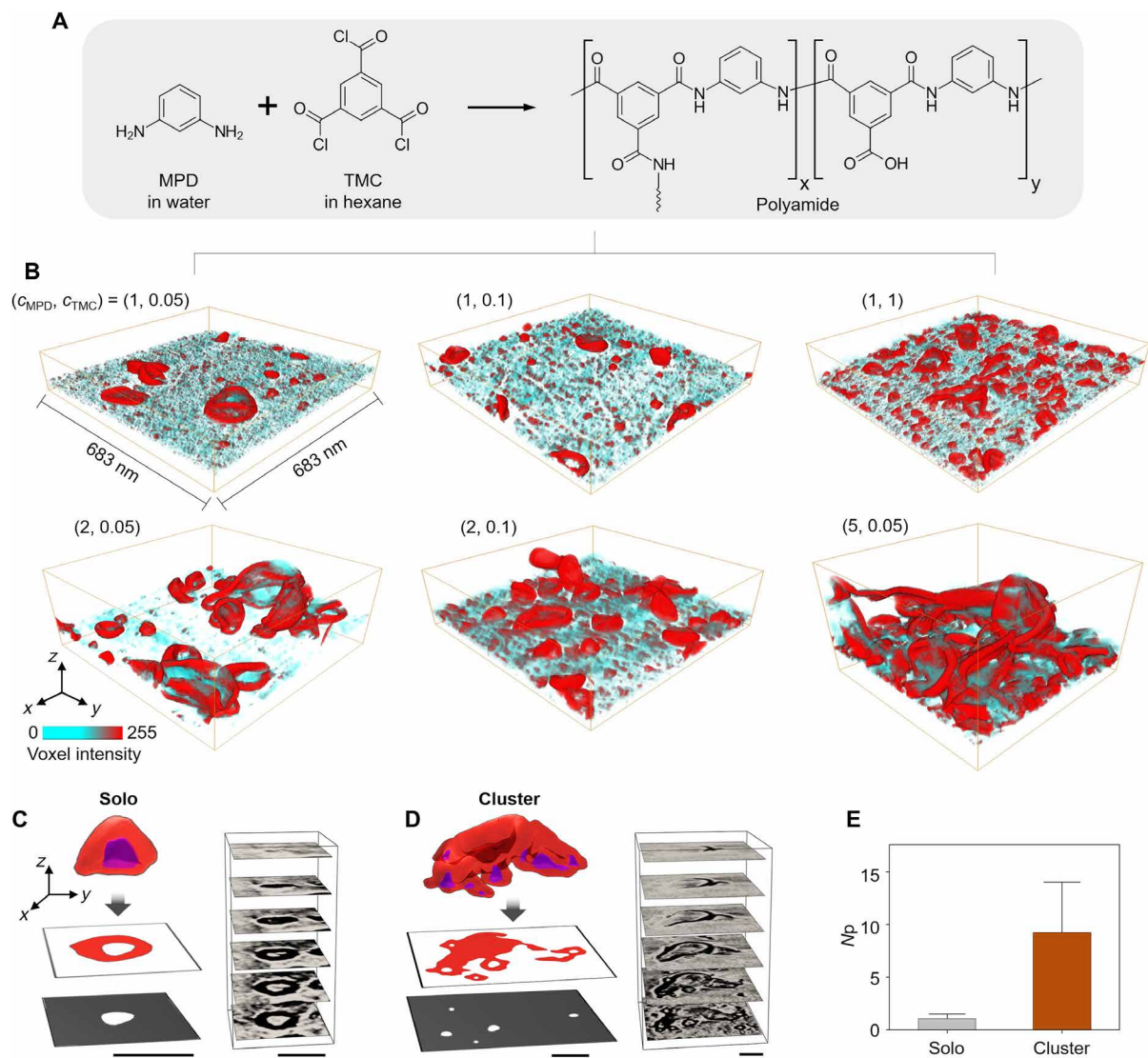
Fig. 1. Tomographic reconstruction of diverse 3D membrane nanostructures produced by variations in the monomer concentrations. (**A**) Interfacial polymerization of MPD and TMC produces crumpled polyamide membranes. (**B**) Full 3D reconstructions of polyamide membranes colored according to the voxel grayscale intensity. MPD and TMC concentrations are given as (c_{MPD}, c_{TMC}) in w/v%. The size of bounding box in (B) is 683 nm by 683 nm (width × length); the height is to scale. (**C** and **D**) Representative examples of (C) a solo crumple and (D) a cluster crumple from the polyamide (1, 1) sample including (top left) 3D reconstructed volumes with void(s) rendered in purple, (middle left) the z-slice of the crumple base, (bottom left) a projected view of the pore(s), and (right) z-slices of the reconstructed tomograms. (**E**) Solo and cluster crumples are differentiated by the number of pores at the base of the crumple (N_p: 1.1 ± 0.4 versus 9.2 ± 4.8, respectively). Scale bars, 50 nm.

previous work has shown that polymer nanofilms can develop structure due to, for example, a thermal gradient to form nanopillars at a molten polymer film (36), acoustic phonons (37), or periodic interfacial thermocapillary stress (35), but these mechanisms involve no molecular reactions and thus are not applicable to our system.

A high areal density of pores is associated with formation of cluster crumples over solo ones during synthesis (Fig. 3A). To illustrate this, alongside whole-membrane views (Fig. 3, B and C), we highlighted clusters in light brown over the pores they envelop (Fig. 3, D and E). As the local areal number density of pores increases [from (1, 0.1) to (1, 1) samples], clustering of multiple adjacent nodules into a single crumple is facilitated by proximity (Fig. 3A and fig. S11). Note that the crumple size normalized by the number of pores

underneath otherwise does not depend on the local areal density as shown in fig. S11. Cluster crumples exhibit phenomenologically larger sizes than solo crumples only because they are effectively multiple crumples merged during growth. Meanwhile, the growth of the crumples can consume MPD and TMC locally and rapidly (24, 26, 38), which may cause the spatial heterogeneity of the concentrations across the polymer film, resulting in the crumple size heterogeneity. On the basis of the Voronoi tessellation of pore positions (Fig. 3, F and G, and fig. S12), the local areal number densities of the pores underneath clusters are higher than those of solo crumples (Fig. 3, H and I). The areal number density of pores is controlled by the monomer concentrations (Fig. 3, J and K), suggesting a multilevel diversification of 3D nanostructures in polyamide membranes: The monomer concentrations dictate the spatial patterns of pores as
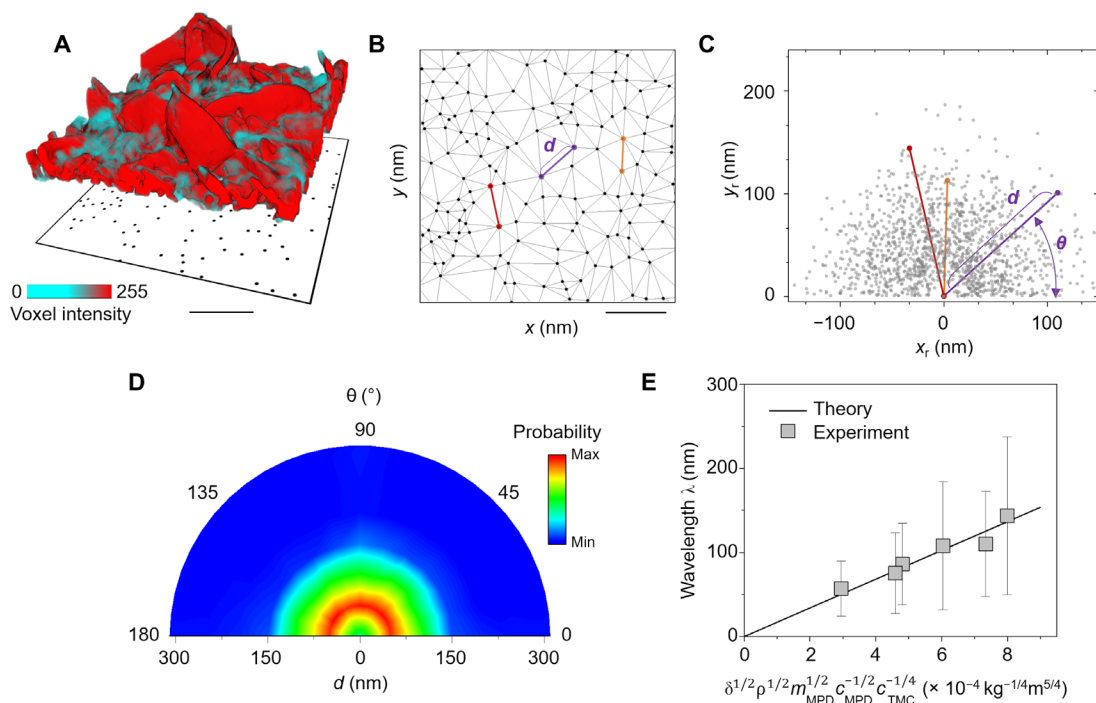
Fig. 2. Spatial patterns of membrane pores are quantitatively tied to monomer concentrations. (**A** to **C**) Workflow of pore pattern wavelength analysis using polyamide (5, 0.05) as an example. (A) Generation of the pore distribution map using the tomogram (fig. S8A), in which the centroid of each pore is marked as a black dot. The pore distribution maps from other membranes are available in fig. S8B. (B) Delaunay triangulation of pore positions, generating a mesh in which the length of each mesh line (examples labeled as red, purple, and orange lines) measures d. (C) Scatter plot of the relative positions of neighboring pores [defined by d and angle θ, labeled in (B) and (C)] from the whole tomogram (fig. S8B). The colored lines (red, purple, and orange) in (C) correspond to the lines in (B). (**D**) Corresponding polar kernel density plot of relative pore positions obtained from (C), showing a clear ring pattern. Its radial profile measures the characteristic wavelength λ (fig. S10 and table S2). The minimum and maximum values of the color bar are 0 and 2.8×10^{-5}, respectively. (**E**) Experimental results (symbols) compared to a linear fit (solid line) based on Eq. 1. The fitted slope is $1.71 \times 10^{-4}\,\mathrm{kg^{1/4}\,m^{-1/4}}$. Error bars represent SDs of the distance histograms in fig. S10. Statistical analysis was done by two-tailed, two-sample unequal variance t test. The t test and a weighted linear fitting confirmed the statistical significance of data (see Materials and Methods for more details). Scale bars, 200 nm.

predicted by Turing's theory, and their density determines the emergence of cluster versus solo crumples.

Relating nanomorphology to membrane permeances

Polyamide membranes were observed to consist of a flat region together with regions with protruding crumples, with the latter relatively increasing the effective membrane surface area. The largest increase in the total surface area of the membrane due to crumpling (152%) was observed for polyamide (2, 0.05), where crumples take up 75.3% of the 2D membrane surface area (Fig. 4A and fig. S13). In addition, the local membrane thickness (Fig. 4, B to D) determines the solvent permeation path length (*11*), which is another morphological parameter that we use in predicting permeances.

From an application standpoint, such a thorough description of membrane surface morphology is of great importance for understanding their separation performance. For example, we found that by using the true surface area and local thickness revealed by tomography, along with the membrane's degree of cross-linking as input for the Spiegler-Kedem model (*39*), we can predict experimental membrane permeance with high accuracy. We show this for membranes synthesized with a range of MPD/TMC concentration ratios. Morphological properties were accounted for via calculation of local thickness for both crumpled and flat regions (Fig. 4, E and F, and fig. S14) and their surface areas. Because the local thickness variation is less than 10% for each membrane sample (table S1), we

used the averaged value of it to represent the membrane thickness. The degree of cross-linking for the membranes [determined by x-ray photoelectron spectroscopy (XPS); fig. S15] for synthesis condition was incorporated to model density changes using literature values (*19*). As shown in Fig. 4G, the resulting model of methanol permeance matched experimental results well (SD of residual permeance was 0.64 liters m⁻² h⁻¹ bar⁻¹ (LMH/bar). Variations in membrane morphology were found to account for 49.3% of modeled permeance, with the remainder being variation of material properties (fig. S16A). In addition, the model fit was notably enhanced when experimental permeance was calculated with the true total surface area (determined by our morphology quantification) compared to the conventional use of the apparent, projected surface area (fig. S16B). Estimation of true membrane surface area more accurately approximates the effective area of a polyamide membrane. We reveal that quantitatively combined understanding of the morphological and materials properties of polyamide membranes is necessary for a physically relevant estimation of permeation performance. Our use of morphological parameters precisely measured from 3D imaging instead of bulk characterizations can be potentially used to correct or develop permeance models.

ML sorts crumples into "morphology groups" with distinct mechanical properties

Despite their apparent heterogeneity, solo crumples can be automatically and robustly sorted into just three subgroups based on
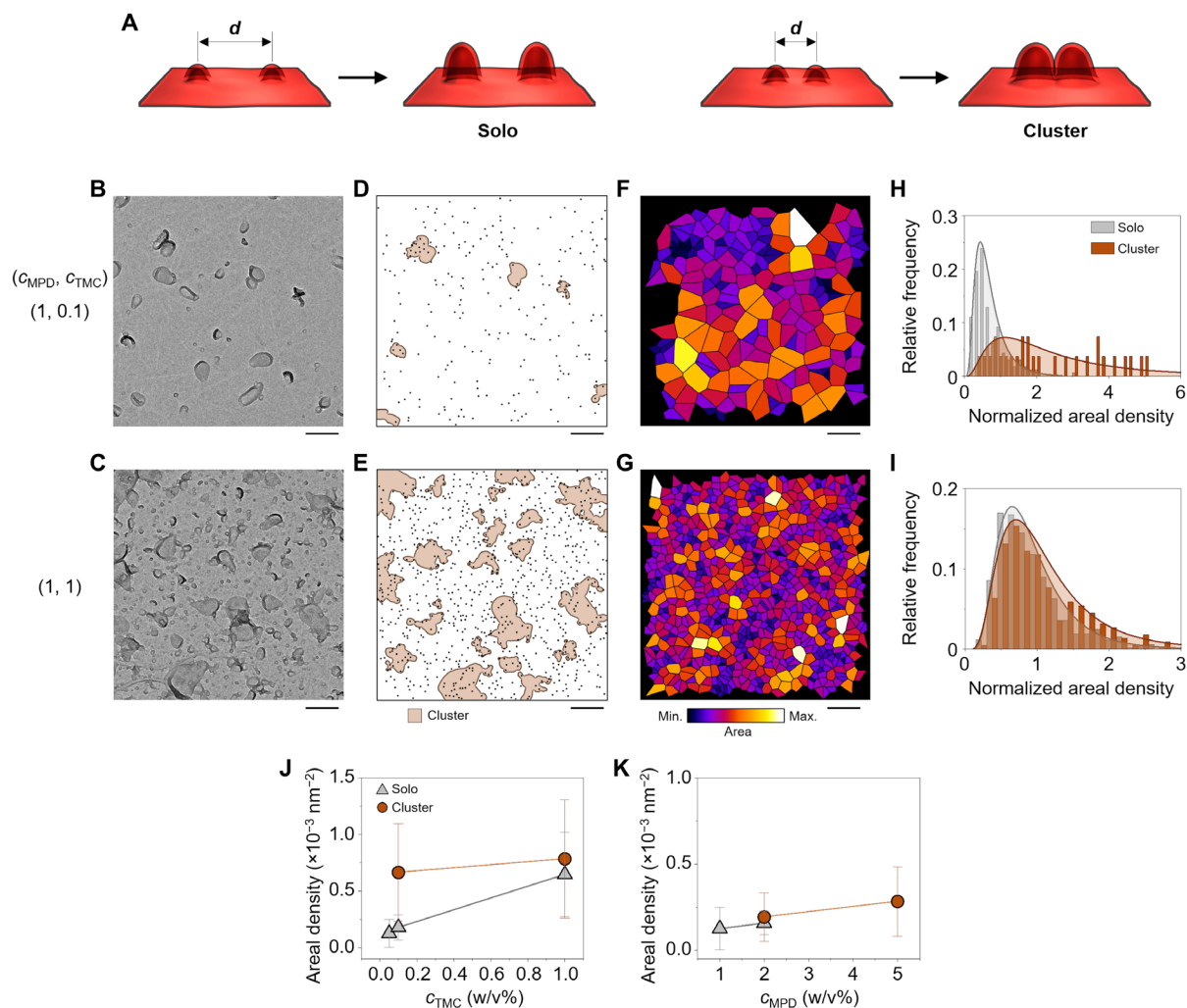
Fig. 3. Synthesis-driven clustering of crumples. (**A**) Schematic illustrations of solo and cluster crumple formation depending on the distance between neighboring pores, *d*. (**B** and **C**) Projection TEM images and (**D** and **E**) corresponding pore maps with clusters highlighted in light brown for the polyamides (1, 0.1) and (1, 1). Location of pores and boundary of clusters are obtained from tomograms. (**F** and **G**) Corresponding Voronoi representations of pore distribution maps colored according to the Voronoi cell area. Voronoi cell area ranges for polyamides (1, 0.1) and (1, 1) are (583 to 2.37×10^4) nm^2 and (257 to 6.13×10^3) nm^2, respectively. (**H** and **I**) Local areal number density of bottom pores (inverse of Voronoi cell area) normalized by the average areal number density of the bottom pores in each synthesis condition. The log-normal fittings in (H) and (I) are to guide the eye. (**J** and **K**) The local areal number density of the pores as a function of (J) c_{TMC} with fixed c_{MPD} (1%) and (K) c_{MPD} with fixed c_{TMC} (0.05%), showing that the pores underneath cluster crumples are denser than those of solo crumples. Statistical analysis was done by two-tailed, two-sample unequal variance *t* test. The *t* test and a weighted linear fitting confirmed the statistical significance of data (see Materials and Methods for more details). Scale bars, 200 nm.

morphometry analysis. Streamlining such a process for irregular 3D shapes is not straightforward, especially since it is hard to identify geometric descriptors that sufficiently represent the shape. We overcame this challenge by developing an ML-based procedure to identify the most important morphological quantities. First, following our previous work (*11*), we converted the surface profiles of the 135 solo crumples into a mesh of 3-nm^2 triangles, from which we collected statistics on local Gaussian curvature (*G*), mean curvature (*H*), curvedness, shape index, and the fractions of tip, tube, valley, and saddle elements across the surface (Materials and Methods, Fig. 5A, and figs. S4 and S17). In parallel, crumple height, surface areas, volumes, and local thickness (the complete list of shape descriptors in table S4 and fig. S18) were extracted from the reconstructed tomographs. All these shape descriptors are applicable to

an arbitrary 3D structure, without fitting to regular shapes such as spheres, ellipsoids, or polyhedra.

Equipped with a much higher dimensional parameter space than our previous work (*11*), we first used an ML-based random forest model to determine the eight most important shape descriptors (Materials and Methods and fig. S19), all of which are related to local crumple curvature. Next, we used principal component analysis (PCA), which requires no prior judgment, to project these eight descriptors into PC space (Fig. 5B) (*40*). The variances of the first two PCs are 85.4 and 7.7%, respectively, demonstrating sufficient dimension reduction while capturing the dominant features (Fig. 5C). These PCs were used to sort the solo crumples into three groups following an unsupervised, ML-based GMM. The three groups—hollow hemispherical domes, elongated but "pinched"
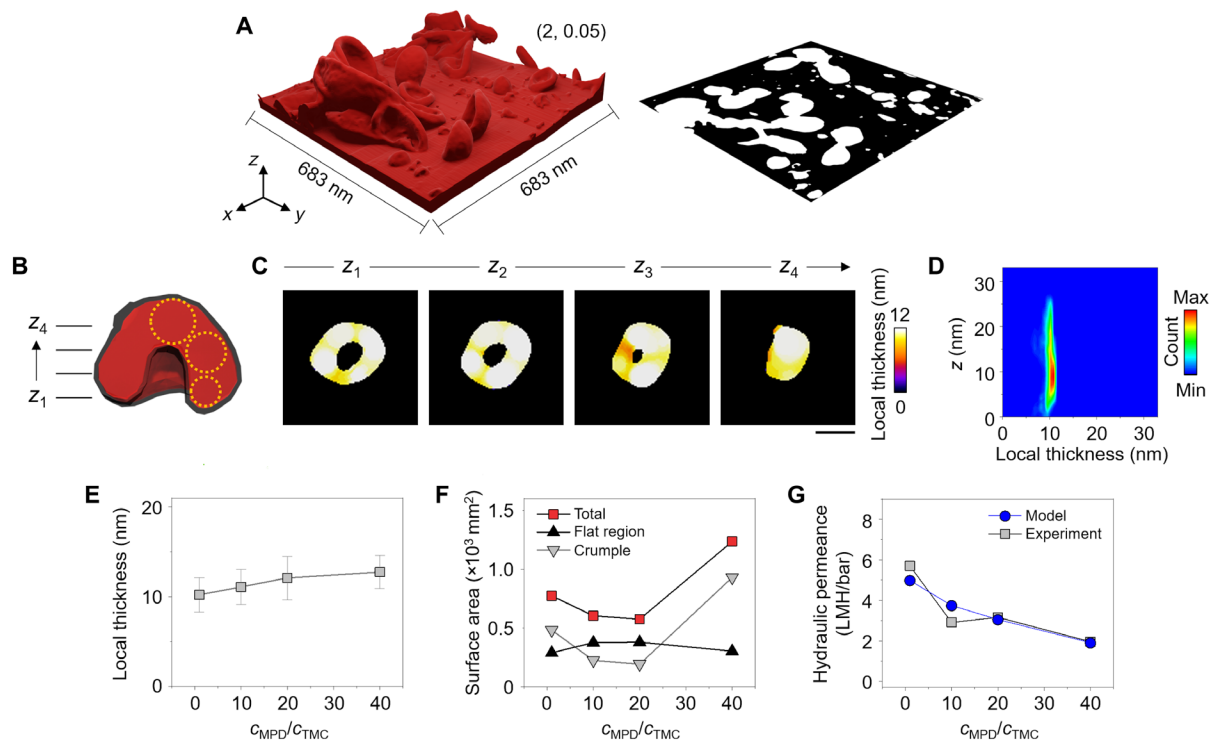
Fig. 4. Quantitative relationship between nanomorphology and methanol permeance. (A) Left: 3D reconstructed volume of polyamide (2, 0.05) to measure the total surface area of the membrane and (A, right) the decoupled surface area of the flat region (black). **(B)** Representative crumple showing the measurement of local thickness at each voxel of the membrane, which is defined as the size of the largest sphere that contains the voxel and remains within the bounds of the membrane (see dotted yellow circles). **(C)** Corresponding z slices of the crumple at a given height colored to the local thickness values. **(D)** Corresponding histogram of local thickness as a function of height. Minimum and maximum values of the color bar are 0 and 770, respectively. **(E)** Local thickness of the crumples and **(F)** surface areas (see fig. S13) as a function of the concentration ratio of MPD to TMC. From left to right: synthesis conditions (c_{MPD}, c_{TMC}): (1, 1), (1, 0.1), (1, 0.05), and (2, 0.05), respectively. **(G)** Experimental measurements and theoretical prediction of methanol permeance of the membranes. Scale bar, 20 nm.

dimples, and flat pancakes (Fig. 5, D to F, and fig. S20)—are present in all but the network membrane sample [polyamide (5, 0.05) in Fig. 1B]. Radar charts of the percentages of tip, tube, valley, and saddle surface elements in the three crumple types (Fig. 5, D to F, bottom) show high consistency across different membranes. Domes always have tips (70 to 80%) as a major surface element, dimples have intermediate levels of tips (40 to 50%) and tubes (20 to 30%), and pancakes have mostly tubes (40 to 50%). The pervasiveness of these morphology groups across synthesis conditions shows that our approach is a reliable way to describe membrane morphology, which we can then relate to the mechanical heterogeneity of membranes (see below). However, the fractions of all four crumple groups (including clusters, Fig. 1, C to E, and the three groups of solo crumples) in a membrane do depend on the monomer concentrations. As shown in Fig. 5G, we applied the morphology grouping workflow to four membrane samples, which show distinct fractions and therefore additional synthetic control over morphology (figs. S21 and S22). We confirmed the reproducibility of our quantitative analysis by conducting the same analysis with the samples synthesized from different batches (fig. S23). While we demonstrated that the thickness and surface area of the membranes determine the permeance performance, we foresee that our quantification of the crumple morphology could allow studies on their possible impacts on solute-membrane interaction and thus the performance regarding solute rejection, selectivity, and even fouling.

The morphology groups identified by our ML analysis are also distinguished by the mechanical microenvironments they present, which is an important consideration given that membranes must endure high hydraulic pressures in reverse osmosis and nanofiltration (*19*), whereas in the past polyamide membranes have been considered to have a single global modulus. To show this, we used liquid-phase AFM to map out the topography and mechanical response of polyamide membranes immersed in water simultaneously for the first time (Fig. 6A). A representative AFM height map of the (2, 0.05) polyamide membrane (Fig. 6B) shows a heterogeneous nanostructure consistent with our TEM data. The AFM tip can simultaneously be used to measure force-indentation curves with 7.8 nm by 7.8 nm lateral resolution and thereby determine a local apparent modulus (Materials and Methods) (*41*). Note that due to the nanoscale rough features exhibited by the membranes and the possibility of bending and flexing of the features, AFM mechanical property test may have a technical difficulty in decoupling mechanical responses from topography properties. Thus, we refer to the modulus values we obtained as apparent modulus in this study. The membrane morphologies are not affected by immersing in water or swelling as shown in comparative AFM analysis and liquid-phase TEM imaging (figs. S24 and S25), which is likely due to the high cross-linking density of the membranes. Figure 6 (G to J) shows that there is nanoscale heterogeneity in the apparent modulus map for all four types of crumples. However, the average crumple moduli are consistent
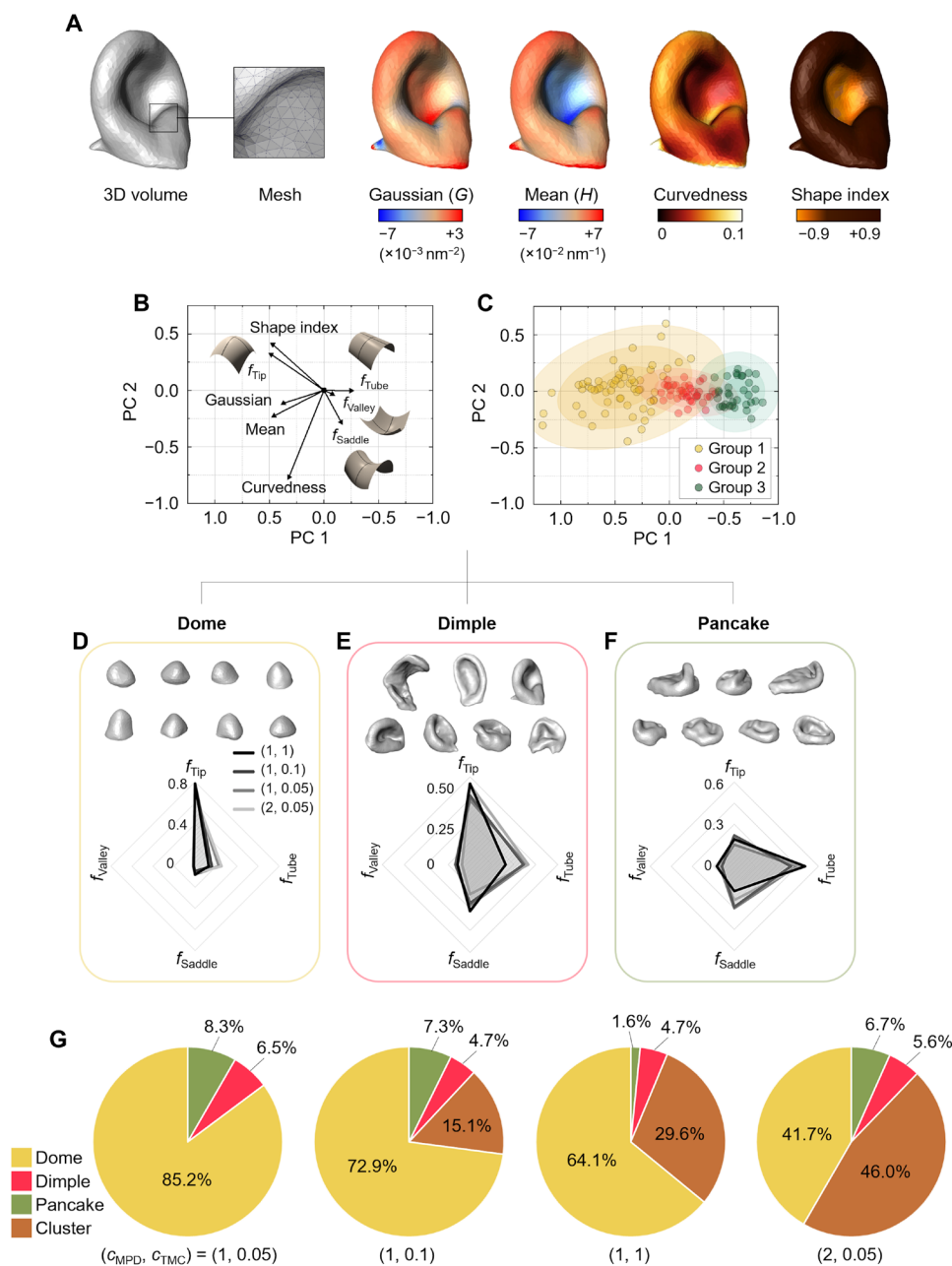
Fig. 5. ML-based nanomorphology grouping of crumples. (**A**) Extraction of shape descriptors on the single-crumple level. From left to right: the segmented volume of a representative crumple, a zoomed-in view of the triangular mesh surface, and the same mesh colored according to different local shape descriptors. (**B**) Shape descriptors projected onto the space of the first two principal components (PCs). Tip, tube, valley, and saddle descriptors are the fractions of these surface elements over the crumple surface (defined in fig. S17B). (**C**) Distribution of the solo crumples projected onto the space spanned by the first two PCs. Color represents the grouping based on a GMM. The colored regions are confidence ellipsoids of the GMM with sigma = 1, 2, and 3. (**D** to **F**, top) Representatives of the three solo crumple morphology groups: (D) domes, (E) dimples, and (F) pancakes. (D to F, bottom) Corresponding radar plots of the fractions of the surface elements (f_{Tip} for tip, f_{Tube} for tube, f_{Valley} for valley, and f_{Saddle} for saddle) for each type of solo crumples (different intensities of gray lines correspond to a different synthesis condition). (**G**) Pie charts of the four crumple types of the polyamide membranes synthesized at different monomer concentrations.

within morphology groups but differ among them (Fig. 6K): The average apparent modulus follows an ascending trend when the crumple type varies from dimples, domes, clusters to pancakes (0.56 ± 0.45, 0.57 ± 0.33, 0.90 ± 0.58, and 0.97 ± 0.58 GPa, respectively). These values are on the same order of magnitude as bulk measurements (*42*, *43*) and now mapped with nanometer resolution. Clusters

have about 60% higher apparent modulus than domes. Dimples have the smallest apparent modulus, which can be attributed to the extended yet partially collapsed shapes, whereas pancakes mostly sit flat with the highest apparent modulus. The modulus AFM measurements show that mechanical heterogeneity exists both on the nanometer scale within a single crumple and across different crumple
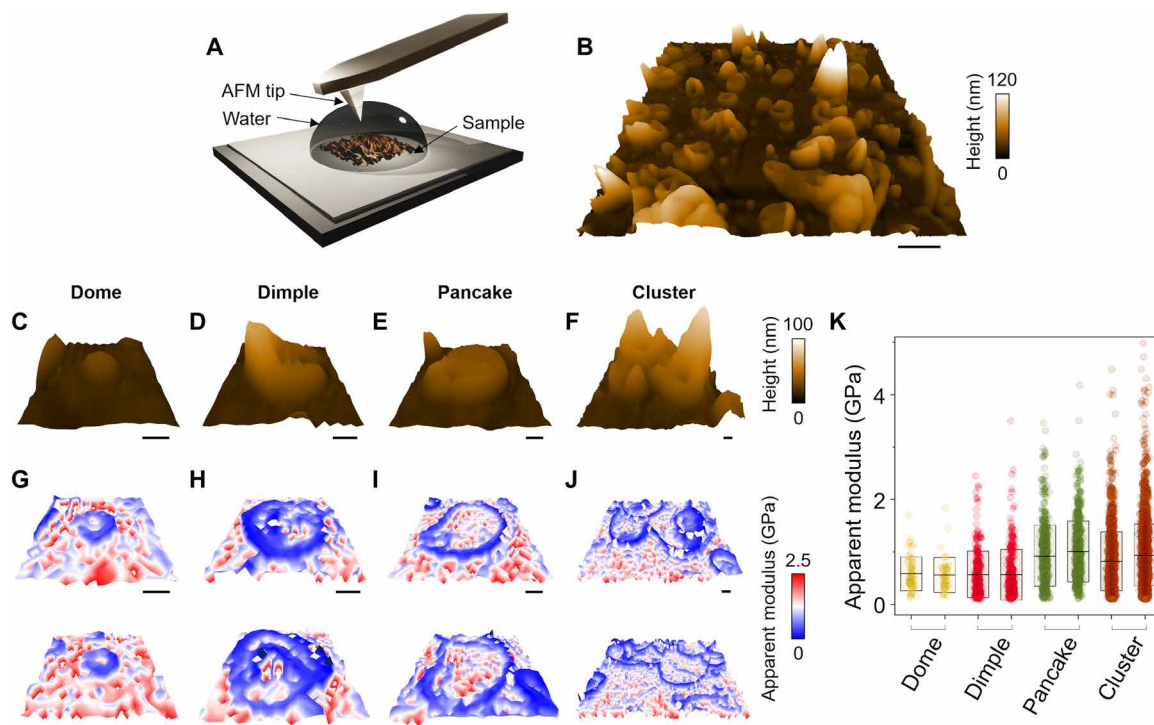
Fig. 6. Crumple morphology groups have distinct nanoscale mechanical heterogeneity. (**A**) Schematic illustration of liquid-phase AFM measurement of a polyamide membrane sample immersed in water. (**B**) 3D-rendered AFM topography image of polyamide (2, 0.05). (**C** to **F**) Representative 3D-rendered AFM topography for representative crumples belonging to the dome, dimple, pancake, and cluster groups. (**G** to **J**) 3D-rendered apparent modulus maps for two typical crumples of each group. From left to right: dome, dimple, pancake, and cluster. Force-indentation curves were recorded from the area spanned by a crumple with a pixel size of 7.8 nm by 7.8 nm, and then the apparent modulus was calculated from the force curves (details in Materials and Methods). (**K**) Apparent modulus obtained from (G) to (J). The box range and middle horizontal line are SD and mean value, respectively. Scale bars, 200 nm in (B) and 50 nm in (C) to (J).

groups, suggesting that synthetically manipulating the relative fractions of these four groups serves as a knob to control the mechanical robustness of polyamide membrane in filtration applications.

DISCUSSION
We used quantitative imaging to understand nanomorphogenesis, including its mechanism and relevance to function, in a model but also industrially relevant soft materials system: polyamide membranes. In doing so, we provide the first quantitative support that crumples protrude under the influence of a reaction-diffusion instability, which determines their areal density in a synthesis-dependent manner. This revelation will aid in predictive design of membrane nanostructures—and therefore performance—by varying the diffusivity, concentration, reactivity, and size of the reactants. It also invites future work in interfacial polymerization systems with other geometries, such as emulsion polymerization schemes used to prepare drug-release microcapsules with morphological and chemical heterogeneity. Our ML workflow to assemble and condense an array of quantitative shape descriptors can be applied to a broad range of amorphous and irregular materials, such as microphase separated polymers and bicontinuous metals (*44*, *45*). Our imaging and analysis methods and the nanomorphogenesis concept can similarly be used in other systems, such as conjugated polymers and composites with different packing morphologies (e.g., nanowhisker and nanoribbons) (*46*, *47*) that have distinct failure modes in flexible electronic and mechanical devices, and nano- or microplastics (*48*)

whose shape could potentially determine their harmfulness to humans. We foresee that our work opens a door to using the middleman of nanostructure to quantitatively and mechanistically link nanomorphologies and functions.

Exciting future improvements can be implemented on both the imaging and analysis sides. For example, combining electron tomography with liquid-phase TEM (*49*) could make it possible to capture continuous movies of nanoscale morphogenesis during the reactions. In addition to the ML-based analysis presented in this work relying on shape descriptors as inputs, it could be greatly advantageous if one could use the reconstructed volume itself as inputs for automated morphology analysis. Coupling with advancements in EM and data science, nanomorphogenesis can become an emerging theme of understanding and designing soft materials.

MATERIALS AND METHODS
Chemicals
Cadmium chloride hydrate (99.998%, $CdCl_2 \cdot xH_2O$, $x \approx 2.5$; Alfa Aesar), ethanolamine (>98%; Sigma-Aldrich), MPD (99%; Sigma-Aldrich), 1,3,5-benzenetricarbonyl trichloride (also known as TMC; 98%, Sigma-Aldrich), molecular sieves (3 Å, 1- to 2-mm beads; Alfa Aesar), hydrochloric acid (36.5 to 38.0%, HCl; Macron), polysulfone film (PS35, Sepro Corporation), potassium hydroxide (KOH), hexanes (99.9%; Fisher Chemical), isopropyl alcohol (IPA), and methanol (99.9%; Fisher Chemical for synthesis, and high-performance liquid chromatography (HPLC) grade, Fisher for permeance test)

were used as received. Approximately 225-g molecular sieves were baked at 110°C in a glass jar for 1 day and then stored with hexane (1 liter). Water used in this study is nanopure water processed by a Milli-Q Advantage A10 system (18.2 megohm·cm at 25°C). All glassware was cleaned with a base bath (saturated KOH in IPA), followed by an acid bath (1 M HCl), thoroughly rinsed with water, and dried with nitrogen gas. Cadmium chloride hydrate, MPD, and TMC were carefully stored in a desiccator to prevent exposure to moisture, which is important for reproducible membrane synthesis.

Polyamide membrane synthesis

Polyamide membranes were synthesized as described previously (19). We used porous sacrificial support layer used to synthesize membranes, which enable precise control of the polyamide layer formation and formation of ultrathin polymer compared to polyamide membrane prepared on conventional support membranes (e.g., polysulfone) having rough and low-porosity surface. A sacrificial support layer of cadmium hydroxide $[Cd(OH)_2]$ nanowires was prepared by sequentially adding aqueous solutions of $CdCl_2 \cdot xH_2O$ (50 ml, 4 mM) and ethanolamine (50 ml, 2 mM) to an Erlenmeyer flask (250 ml). The solution was stirred with a Teflon-coated magnetic stir bar (2 cm long) at 500 rpm at room temperature for 15 min and turned cloudy. The polysulfone substrate (6 cm by 6 cm), having been stored in water for 12 hours, was fixed on a glass filter funnel (3.8 cm inner diameter) connected to a filtering flask, which was connected to a vacuum pump (KNF, UN726.3 FTP). The polysulfone substrate was washed by filtering 20 ml of methanol, followed by filtering 50 ml of water under vacuum. The solution of $Cd(OH)_2$ nanowires was filtered across the polysulfone substrate with a vacuum pressure of −67 kPa. An aqueous solution of MPD with the desired concentration (c_{MPD}, from 1 to 5 w/v%) was then gently transferred onto the nanowire-coated polysulfone using a 10-ml micropipette and filtered with a vacuum pressure of −67 kPa. The filtering was stopped once the $Cd(OH)_2$ nanowire layer was just wet with the MPD solution. Hereafter, we will use % to designate only weight per volume percent (i.e., gram per milliliter, w/v%). A TMC solution in hexane with the desired concentration (c_{TMC}, from 0.05 to 1%) was gently transferred onto the polysulfone substrate. Interfacial polymerization initiates immediately upon contact of the MPD and TMC solutions. After 60 s, the TMC solution was gently removed using a micropipette and then pure hexane (10 ml) was added to rinse away excess TMC. This rinsing step was repeated two more times. Immediately afterward, the polysulfone substrate covered with the synthesized polyamide membrane was placed in a water-filled petri dish (10 cm in diameter). The polyamide membrane separates from the polysulfone substrate and floats at the air-water interface. The water in the petri dish was then replaced with a dilute HCl solution (10 mM) using a micropipette. The polyamide membrane was kept floating on the dilute HCl solution overnight to remove any residue of the $Cd(OH)_2$ nanowires. The HCl solution was then replaced with water five times before the membrane was scooped onto a carbon film–coated TEM grid (Electron Microscopy Sciences, CF400-Cu). Note that the membranes are overall flat on the TEM grid without wrinkles or cracks introduced during the transferring process from liquid to TEM grids. This is consistently confirmed in TEM (figs. S1, S2, and S23), SEM (fig. S6), and AFM (Fig. 6B and fig. S14), all samples of which follow the same sample preparation procedure of first etching $Cd(OH)_2$

sacrificial layer and then scooping the membrane using a solid substrate. The membrane was dried in air for TEM imaging.

Chemical characterization of polyamide membrane with XPS

Free-standing membranes were transferred to silicon wafers, and XPS (Kratos Axis) was performed using an Al K-α X-ray (source energy of 1486.6 eV). All spectra were collected at a pass energy of 160 eV and at an energy step size of 1 eV. A linear-type background subtraction was applied to the photoemission lines. The degree of cross-linking was calculated from the Os1 and Ns1 portion of the photoemission spectrum using the equations below (19)

$$Os1/Ns1 = \frac{(3X + 4Y)}{(3X + 2Y)} \tag{3}$$

$$DOC = \frac{X}{X + Y} \times 100\% \tag{4}$$

where $Os1$ and $Ns1$ are the integrated peak areas for Os1 and Ns1, respectively. X and Y are the number portion of cross-linked and linear structures, respectively. DOC is the degree of cross-linking. The mass fraction of MPD in a membrane, m_{MPD}, was estimated using the equation below

$$m_{MPD} = X m_{MPD,network} + Y m_{MPD,linear} \tag{5}$$

where $m_{MPD, network}$ and $m_{MPD, linear}$ are mass fractions of MPD in cross-linked and linear structures, respectively.

Polyamide membrane imaging by TEM

A JEOL 2100 Cryo TEM at an acceleration voltage of 200 kV was used for TEM imaging of the polyamide membranes. Low electron dose rates (4 to 7 $e^- Å^{-2} s^{-1}$) were applied using spot size 3 to minimize beam-induced alteration. For tomography, we prepared six polyamide membranes, with c_{MPD} and c_{TMC} systematically varied: c_{MPD} of 1, 2, or 5% with a fixed c_{TMC} of 0.05%; c_{TMC} of 0.05 or 0.1% with a fixed c_{MPD} of 1%; and c_{MPD} of 2% and c_{TMC} of 0.1%. Note that the two monomers were shown to have a competing effect on membrane nanomorphology in our previous work, by scaling the morphological parameters obtained from 2D TEM images as a function of the monomer concentrations or the concentration ratio (50). Thus, we choose six conditions (three with varied c_{MPD} at a fixed c_{TMC} of 0.05%, two with varied c_{TMC} at a fixed c_{MPD} of 1%, and one with c_{MPD} of 2% and c_{TMC} of 0.1%) to study the effect of monomer concentrations in 3D structure of crumples in this study. These six membranes also exhibit individual and separable crumples, which allow for a unified analysis framework for quantitative comparison. For each polyamide film, a total of 61 tilt images were acquired over a tilt range of −60° to +60° with an angle increment of 2° (fig. S2). Each image was collected with an exposure time of 1 s, resulting in a dose per image of 4 to 7 $e^- Å^{-2}$. The sample was set to its eucentric height at each tilt angle manually, followed by a defocus of −2048 nm to improve contrast, and the same defocus was used throughout all tilt series acquisition. TEM images were aligned and assembled using the patch tracking module in the open-source software IMOD 4.9.3 (University of Colorado, http://bio3d.colorado.edu/) (51). After the alignment, the tomograms of these samples (Fig. 1B) were generated using the Model-Based Iterative Reconstruction (MBIR) algorithm with diffuseness of 0.3 and smoothness of 0.2 (43).

Polyamide membrane imaging by SEM

A Hitachi S4800 High-Resolution SEM was used for SEM imaging of the polyamide membranes. A small Si wafer (5 mm by 5 mm) was used as the SEM sample substrate, which was first cleaned with water, acetone, and isopropanol, and then treated with oxygen plasma for 1 min. For the top surface sample, we scooped the membrane floated on the water surface with the Si wafer. For the bottom surface sample, the Si wafer was flipped with its surface approaching toward the top surface of the membrane floated on the water surface. Both SEM samples were dried in air. The samples were coated with a thin film of Au-Pd by sputter coating before SEM characterization.

Polyamide membrane imaging by graphene liquid cell

Graphene liquid cell TEM imaging of polyamide membrane was conducted on a JEOL 2100 Cryo TEM at an acceleration voltage of 200 kV. Preparation of the graphene liquid cells follows previous literature (52), with the modification that we used one graphene-coated TEM grid to scoop a small piece (~1 mm by 1 mm) of polyamide membrane floated on the water surface. Because water wets the membrane well, a thin water film was scooped together on top of the membrane. Next, the other graphene-coated TEM grid was applied to overlay on top of the membrane and the water film to complete the sealing.

Analysis of the 3D tomograms of the polyamide membranes

Segmentation and morphology analysis of reconstructed membranes were performed in ImageJ/FIJI (53) and Amira 6.4 (FEI) (54). ImageJ/FIJI was used to analyze the pore distribution. The pores underneath each nodule were identified by scanning for voids in the bottom few z-slices of the tomograms and used to generate a pore distribution map (Fig. 2A). For segmentation and 3D morphology analysis, the reconstructed tomograms were imported into Amira. For segmentation, a median filter over a $3 \times 3 \times 3$ voxel neighborhood and 26 iterations were applied, followed by a 3D Gaussian filter with a kernel size of 9 in 3D with SD voxel of $3 \times 3 \times 3$ and then a 3D edge-preserving smoothing filter with 25 time, 5 step, 3.5 contrast, and 3 sigma. Contrast and brightness were not adjusted. A grayscale threshold was set on a per-sample basis to generate an approximately segmented volume, which was then corrected using a manual adjustment to fill in holes or remove regions not corresponding to the crumple. These procedures of segmentation were repeated for four polyamide membranes: c_{MPD} of 1 and 2% with a fixed c_{TMC} of 0.05% and c_{TMC} of 0.05 and 0.1% with a fixed c_{MPD} of 1%.

To extract crumple shape descriptors, individual crumples were first cropped from the segmented tomographs. The volume, height, external surface area, sphericity, and surface area–to–volume ratio of the crumples were measured using the MorphoLibJ plugin of ImageJ (55). We also quantified morphology parameters of the pores themselves including perimeter, (2D) area, equivalent radius, maximum Feret distances (i.e., the longest distances between two parallel lines restricting the boundary of each pore), aspect ratio, and circularity ($4\pi \times$ (area)/(perimeter)^2) using the BioVoxxel Image Processing and Analysis Toolbox for ImageJ. The local thickness of crumples was measured using the Local Thickness plugin of ImageJ (56). Uni- or bimodal distributions were observed for the crumple local thickness δ (fig. S18), and the first peak was used as the local thickness in the main. We attribute the second peak to regions where two parts of the membrane are arranged such that they touch. Amira was used for the analysis of crumple surface curvatures. Segmented crumples were converted to a network of triangular meshes using the Generate Surface function with 1/16 simplification for all the crumples. The meshed network was smoothed using the Smooth Surface function with four iterations and lambda of 0.7. Principal curvatures (κ_1, κ_2) are defined as $1/R_1$ and $1/R_2$, where R_1 and R_2 are the radii of the smallest and largest spheres, respectively, that can be fit to the surface at each mesh point. The Gaussian (G) and mean (H) curvatures are $G = \kappa_1\kappa_2$ and $H = (\kappa_1 + \kappa_2)/2$. Curvature elements (tube, saddle, tip, and valley) at each mesh were determined using the arithmetic function

$$(\kappa_1 > 0\,\&\&\,\kappa_2 > i) + 2(\kappa_1 > 0\,\&\&\,\kappa_2 < i\,\&\&\,\kappa_2 < j) + 3(\kappa_1 > 0\,\&\&\,\kappa_2 < j) + 4(\kappa_1 < 0\,\&\&\,\kappa_2 < j) \tag{6}$$

where && is the Boolean "and." Thus, the expression returns 1 for a "tip" element, 2 for a "tube" element, 3 for a "saddle" element, and 4 for a "valley" element. Thresholds i and j were chosen as 0.005 and −0.005 because the second principal curvature (and therefore G) at tube elements is never perfectly zero (i.e., the film is never perfectly flat). The curvedness (C) and shape index (SI) are $C = \sqrt{(\kappa_1^2 + \kappa_1^2)/2}$ and SI = $(2/\pi)\tan^{-1}((\kappa_1 + \kappa_2)/(\kappa_1 - \kappa_2))$.

PCA and GMM-based grouping of crumple morphologies

The 135 solo crumples identified in the pore analysis process were first manually classified into three groups simply based on the apparent appearance of their morphologies without rigorous geometrical criteria. Then, using all 49 shape descriptors (table S4) we obtained as the input and the manual classification labels as output, we trained a random forest classifier to predict the classes of the crumples. The random forest classifier model has 200 estimators, a feature maximum of 7, and a depth maximum of 20. With the validation split of 0.8, we cross-validated the random forest model 100 times and the result showed an average accuracy of 83.2 ± 6.0%, matching with the manual classification labels. We then plotted out the ranking of the importance of all the shape descriptors, which was computed as the (normalized) total reduction of the Gini impurity brought by that descriptor (also known as the Gini importance) (fig. S19) (57). In doing so, we identified eight important and systematic shape descriptors including the curvedness, Gaussian curvature, mean curvature, and shape index averaged over all the meshes of a crumple, and ratios of tip, tube, saddle, and valley elements on crumple surfaces, which were further used for the PCA dimension reduction. The averaged curvedness, Gaussian curvature, mean curvature, and shape index were normalized across 135 solo crumple samples by the following equation

$$N_{normalized} = \frac{N - \min(N)}{\max(N) - \min(N)} \tag{7}$$

where N denotes one shape descriptor. Then, the normalized eight parameters of 135 solo crumples were projected into first two PC space by PCA. The variances of first two PCs are 85.4 and 7.7%. Then, the dimension reduced data points were clustered with a GMM (58) with three centers. Random forest, PCA, and Gaussian mixture modeling were done in Python using scikit-learn.

Quantitative analysis of the pore patterns by Turing's theory

On the basis of the one-to-one relation of crumple-bottom pore, we focus on the average distance between pores for each synthesis

condition, which can be interpreted as the characteristic wavelength of a Turing structure λ and is given by

$$\lambda = (2\pi\tau D)^{1/2} \tag{8}$$

where D is the geometric average diffusion coefficient of the reactants, $D = (D_{MPD}D_{TMC})^{1/2}$. Because the reaction diffusion process for this system happens mainly in the hexane phase, D_{MPD} and D_{TMC} represent the diffusion coefficients of MPD and TMC in hexane, respectively, and τ is the period of the cycle oscillation when the system is at the onset of a Hopf bifurcation (59). Here, we estimate τ as the formation time of the membrane since the interfacial polymerization reaction is extremely rapid (31). This time scale is expected to follow

$$\tau \sim \frac{M}{J} \tag{9}$$

where M is the total mass of MPD molecules per unit area in the formed membrane and J is the the mass flux of MPD. M is proportional to the local thickness δ of the membrane measured in our experiments, the polymer density ρ, and the mass fraction, m_{MPD}, of MPD in the membrane; thus, $M \sim \delta\rho m_{MPD}$. Polymer density is related to the degree of polymer cross-linking (DOC) when temperature, reaction time, and membrane synthesis technique are all held constant. The linear correlation of DOC (estimated from XPS; fig. S15) with polymer density ρ was used to estimate ρ based on the following, using literature values (19, 32)

$$\rho = DOC \times \left(3.39\frac{g}{ml}\right) - 1.58\frac{g}{ml} \tag{10}$$

Note that the correlation in these references was based on a linear regression of data and only applicable within a DOC range of 0.6 to 0.95, which is the case for our data.

At short time scales, it has been suggested that the reaction is dominated by monomer-monomer coupling in the reaction-diffusion boundary layer (25), and thus, J follows

$$J \sim c_{MPD}(c_{TMC}D_{MPD})^{1/2} \tag{11}$$

From Eqs. 8, 9, and 11, we obtained

$$\lambda \sim \delta^{1/2}\rho^{1/2}m_{MPD}^{1/2}D_{TMC}^{1/4}c_{MPD}^{-1/2}c_{TMC}^{-1/4} \tag{12}$$

In addition, the interfacial polymerization time τ in our experiment can be estimated from Eqs. 8 and 12 as

$$\tau = \frac{\lambda^2}{2\pi(D_{TMC}D_{MPD})^{1/2}} \sim \delta\rho\, m_{MPD}c_{MPD}^{-1}c_{TMC}^{-1/2}D_{MPD}^{-1/2} \tag{13}$$

Statistics
Two-tailed, two-sample unequal variance t test and linear regression analysis on spatial patterns and local areal number density of membrane pores related to monomer concentrations were performed using Microsoft Excel (version 2102) and Software OriginPro 2020 (version 9.7.0.188). A P value for F test < level of significance ($\alpha = 0.05$) was considered significant.

Estimation of Rayleigh number (Ra) and Marangoni number (Ma)
The following equations define the Rayleigh number and Marangoni number (34)

$$Ra = g\beta\Delta T\delta^3/(\eta\alpha) \text{ and } Ma = -\gamma_T\Delta T\delta/(\rho_l\eta\alpha) \tag{14}$$

where $g = 9.81$ m s^{-2} is the gravitational acceleration; β, ρ_l, η, and α are the thermal expansion coefficient, density, kinematic viscosity, and thermal diffusivity of the liquid, respectively; $\gamma_T \equiv |d\gamma/dT|$ is the interfacial tension change rate with the temperature; and ΔT is the temperature difference across the membrane thickness δ. In the experimental system for the polyamide membrane formed in hexane (31), $\beta = 1.48 \times 10^{-3}$ K^{-1}, $\eta = 4.55 \times 10^{-7}$ m$^{2-1}$ s^{-1} (19), $\alpha = 7.89 \times 10^{-8}$ m^2 s^{-1} (19), $\gamma_T \approx -10^{-4}$ N m^{-1} K^{-1} (60), and $\rho_l = 655$ kg m^{-3} (61). In a crumpled structure $\delta \approx 10^{-8}$ m and $\Delta T \sim \mathcal{O}(10$ K$)$ (27), $Ra \sim \mathcal{O}(10^{-12})$ and $Ma \sim \mathcal{O}(10^{-1})$.

Mechanical response mapping
Liquid-phase AFM measurements were performed using an Asylum Cypher S AFM. A small Si wafer (5 mm by 5 mm) was used as the AFM sample substrate, which was first cleaned with water, acetone, and isopropanol, and then treated with oxygen plasma for 1 min. The AFM sample was prepared by scooping the as-synthesized membrane with the Si wafer and allowing it to dry in air. The Si wafer was mounted onto the sample stage in the microscope under ambient conditions. A droplet of water was added onto the surface of the membrane right before the AFM measurements. The model of the AFM tip is Multi75-G from BudgetSensors, with a typical spring constant of 2.2 N m^{-1}. The spring constant of the AFM tip was measured via thermal tune to ensure an accurate measurement of the force, while the inverse optical lever sensitivity was calibrated on the basis of the force-distance curves collected on a clean Si wafer. Fast force mapping (FFM) was performed with a Z-rate (vertical force spectra) of 200 Hz and a lateral pixel size of 7.8 nm. The height image, modulus map, and force curves at different locations were obtained on the basis of the FFM results. The reported apparent modulus was based on the fitting results using Hertz model with bottom-effect correction (41, 62). The corrected force can be expressed as

$$F_{corrected} = \frac{4E\sqrt{l^3 r}}{3(1-v^2)}\left[1 - \frac{2f_0\sqrt{lr}}{\pi h} + \frac{4f_0^2 lr}{\pi^2 h^2} - \frac{8(f_0^3 + 4\pi^2 g_0/15)lr\sqrt{lr}}{\pi^3 h^3} + \frac{16f_0(f_0^3 + 3\pi^2 g_0/5)l^2 r^2}{\pi^4 h^4}\right] \tag{15}$$

where E is the modulus, r is the AFM tip radius, l is the indentation depth, h is the sample height measured by AFM at each pixel, and the constants f_0 and g_0 are functions of the sample Poisson's ratio v. For a sample not bonded to the substrate, f_0 and g_0 can be expressed as

$$f_0 = -0.347\frac{3-2v}{1-v}, g_0 = 0.056\frac{5-2v}{1-v} \tag{16}$$

We approximated the tip as a sphere with a radius of 7 nm, a Poisson's ratio of 0.17, and a modulus of 150 GPa, and estimated the membrane's Poisson's ratio to be 0.39, as the fitting parameters for Eqs. 15 and 16.

Methanol permeance testing

The methanol permeability for all membranes was measured with an electronically controlled pressure-driven membrane testing cell (Sterlitech HP4750). Membranes with a 25 mm diameter were given 24 hours to soak in methanol (HPLC-grade, Fisher Chemical) before testing. The presoaked membrane was quickly and carefully loaded into the Sterlitech cell with the support layer of the membrane facing the outlet. Throughout membrane loading, the membrane remained saturated with methanol. The input compartment of the Sterlitech cell was filled with 100 ml of methanol and fully assembled. An electronically controlled nitrogen manifold was then connected via the top of the input solution compartment of the cell, and the output side of the Sterlitech cell was connected to a thin hose going to a collection container atop a mass balance.

Once the testing apparatus was assembled, a permeability measurement experiment was controlled with a LabVIEW interface. The experiment was initialized by electronically opening the main nitrogen valve, which allowed the regulated nitrogen supply to gradually pressurize the methanol containing input compartment of the flow cell to 150 psi. Pressure was slowly built up to 150 psi within the cell with a throttling valve. The flow rate of the methanol permeate was calculated from the change in mass of the collection container over time—pressure and mass data were recorded every second. The apparatus was operated until 80% of the initial 100 ml of methanol had permeated through the membrane. Next, the pressure was slowly released, and the tested membrane was removed and stored once dry.

Membrane permeance was calculated using the equation below

$$\text{Permeance} = \frac{\dot{M}}{A \times P} \tag{17}$$

where $\dot{M}$ is the average mass flow rate of methanol through the cell, A is the membrane area, and P is the applied pressure.

Modeling membrane permeance from morphology and density data

First, the surface areas of crumple region and flat region were decoupled using Blender 2.9 (Blender Foundation) and then the fraction of crumpled area over total surface area (x_{cr}) was calculated for the membrane synthesized at each concentration ratio of MPD to TMC ($k = 1, 10, 20,$ and 40) from morphology data using the following equation

$$x_{cr,k} = \frac{A_{cr,k}}{A_{cr,k} + A_{fl,k}} \tag{18}$$

where A_{cr} is the measured surface area of the crumple region and A_{fl} is the measured surface area of flat membrane region (fig. S13).

The nominal membrane thickness ($\delta_{nom,k}$) for each monomer ratio was then calculated using the local thickness of crumpled region ($\delta_{cr,k}$; Fig. 4, B to E) and the flat region thickness ($\delta_{fl,k}$; fig. S14D), assuming that there is a purely bimodal distribution of thickness for the membrane (fig. S18)

$$\delta_{nom,k} = \left[\frac{x_{cr,k}}{\delta_{cr,k}} + \frac{1 - x_{cr,k}}{\delta_{fl,k}} \right]^{-1} \tag{19}$$

The solvent-membrane permeability (P_m) was then calculated for each monomer ratio given the nominal membrane thickness and experimentally determined solvent permeance (L_p^{exp}) with the following equation

$$P_{m,k} = L_{p,k}^{exp} \times \delta_{nom,k} \tag{20}$$

To build a model of the system ignoring the role of material properties like mass density (this model is given notation mod1), the solvent-membrane permeability for each monomer ratio, k, was averaged ($P_{m,avg}$). Solvent permeance, L_p^{mod1}, was then calculated using

$$L_{p,k}^{mod1} = P_{m,avg}/\delta_{nom,k} \tag{21}$$

By holding permeability constant, mod1 assumes only the thickness of the membrane changes with monomer ratio.

For model 2 (mod2), permeance was assumed to be dependent on the mass density of the polyamide membranes as well. Solvent-membrane permeability is inversely proportional to membrane density; therefore, to isolate the effects of density on permeability, a permeability constant, μ, defined as follows was calculated for each monomer ratio

$$\mu_k = P_{m,k} \times \rho_k \tag{22}$$

The permeability constant, μ, for each monomer ratio was averaged to form μ_{avg}. For mod2, only surface area, membrane thickness, and polymer density were accounted for by defining μ_{avg} as constant for all monomer ratios in the following equation of solvent permeance

$$L_{p,k}^{mod2} = \frac{\mu_{avg}}{\rho_k \times \delta_{nom,k}} \tag{23}$$

Models 1 and 2 are compared in fig. S16.

SUPPLEMENTARY MATERIALS

REFERENCES AND NOTES

1. R. Gordon, D. Losic, M. A. Tiffany, S. S. Nagy, F. A. S. Sterrenburg, The glass menagerie: Diatoms for novel applications in nanotechnology. *Trends Biotechnol.* **27**, 116–127 (2009).
2. P.-F. Xu, N. Houssin, K. F. Ferri-Lagneau, B. Thisse, C. Thisse, Construction of a vertebrate embryo from two opposing morphogen gradients. *Science* **344**, 87–89 (2014).
3. S. Hu, K. Dasbiswas, Z. Guo, Y.-H. Tee, V. Thiagarajan, P. Hersen, T.-L. Chew, S. A. Safran, R. Zaidel-Bar, A. D. Bershadsky, Long-range self-organization of cytoskeletal myosin II filament stacks. *Nat. Cell Biol.* **19**, 133–141 (2017).
4. F. H. Wilt, Developmental biology meets materials science: Morphogenesis of biomineralized structures. *Dev. Biol.* **280**, 15–25 (2005).
5. C. N. Kaplan, W. L. Noorduin, L. Li, R. Sadza, L. Folkertsma, J. Aizenberg, L. Mahadevan, Controlled growth and form of precipitating microsculptures. *Science* **355**, 1395–1399 (2017).
6. A. S. Gladman, E. A. Matsumoto, R. G. Nuzzo, L. Mahadevan, J. A. Lewis, Biomimetic 4D printing. *Nat. Mater.* **15**, 413–418 (2016).
7. M.-J. Gim, D. A. Beller, D. K. Yoon, Morphogenesis of liquid crystal topological defects during the nematic-smectic A phase transition. *Nat. Commun.* **8**, 15453 (2017).
8. Y. Li, N. Khuu, E. Prince, M. Alizadehgiashi, E. Galati, O. D. Lavrentovich, E. Kumacheva, Nanoparticle-laden droplets of liquid crystals: Interactive morphogenesis and dynamic assembly. *Sci. Adv.* **5**, eaav1035 (2019).
9. P. S. Singh, S. Joshi, J. Trivedi, C. Devmurari, A. P. Rao, P. Ghosh, Probing the structural variations of thin film composite RO membranes obtained by coating polyamide over polysulfone membranes of different pore dimensions. *J. Membr. Sci.* **278**, 19–25 (2006).
10. L. Lin, C. Feng, R. Lopez, O. Coronell, Identifying facile and accurate methods to measure the thickness of the active layers of thin-film composite membranes–A comparison of seven characterization techniques. *J. Membr. Sci.* **498**, 167–179 (2016).
11. X. Song, J. W. Smith, J. Kim, N. J. Zaluzec, W. Chen, H. An, J. M. Dennison, D. G. Cahill, M. A. Kulzick, Q. Chen, Unraveling the morphology–function relationships of polyamide membranes using quantitative electron tomography. *ACS Appl. Mater. Interfaces* **11**, 8517–8526 (2019).

12. T. E. Culp, Y.-X. Shen, M. Geitner, M. Paul, A. Roy, M. J. Behr, S. Rosenberg, J. Gu, M. Kumar, E. D. Gomez, Electron tomography reveals details of the internal microstructure of desalination membranes. *Proc. Natl. Acad. Sci. U.S.A.* **115**, 8694–8699 (2018).

13. F. Pacheco, R. Sougrat, M. Reinhard, J. O. Leckie, I. Pinnau, 3D visualization of the internal nanostructure of polyamide thin films in RO membranes. *J. Membr. Sci.* **501**, 33–44 (2016).

14. T. E. Culp, B. Khara, K. P. Brickey, M. Geitner, T. J. Zimudzi, J. D. Wilbur, S. D. Jons, A. Roy, M. Paul, B. Ganapathysubramanian, M. Kumar, E. D. Gomez, Nanoscale control of internal inhomogeneity enhances water transport in desalination membranes. *Science* **371**, 72–75 (2021).

15. A. H. Gröschel, A. H. E. Müller, Self-assembly concepts for multicompartment nanostructures. *Nanoscale* **7**, 11841–11876 (2015).

16. R. Chelakkot, L. Mahadevan, On the growth and form of shoots. *J. R. Soc. Interface* **14**, 20170001 (2017).

17. N. L. Nerurkar, L. Mahadevan, C. J. Tabin, BMP signaling controls buckling forces to modulate looping morphogenesis of the gut. *Proc. Natl. Acad. Sci. U.S.A.* **114**, 2277–2282 (2017).

18. P. Marchetti, M. F. Jimenez Solomon, G. Szekely, A. G. Livingston, Molecular separation with organic solvent nanofiltration: A critical review. *Chem. Rev.* **114**, 10735–10806 (2014).

19. S. Karan, Z. W. Jiang, A. G. Livingston, Sub–10 nm polyamide nanofilms with ultrafast solvent transport for molecular separation. *Science* **348**, 1347–1351 (2015).

20. M. C. Y. Wong, L. Lin, O. Coronell, E. M. V. Hoek, G. Z. Ramon, Impact of liquid-filled voids within the active layer on transport through thin-film composite membranes. *J. Membr. Sci.* **500**, 124–135 (2016).

21. H. Yan, X. Miao, J. Xu, G. Pan, Y. Zhang, Y. Shi, M. Guo, Y. Liu, The porous structure of the fully-aromatic polyamide film in reverse osmosis membranes. *J. Membr. Sci.* **475**, 504–510 (2015).

22. A. M. Turing, The chemical basis of morphogenesis. *Philos. Trans. R. Soc. B* **237**, 37–72 (1952).

23. J. Muscatello, E. A. Müller, A. A. Mostofi, A. P. Sutton, Multiscale molecular simulations of the formation and structure of polyamide membranes created by interfacial polymerization. *J. Membr. Sci.* **527**, 180–190 (2017).

24. A. Nowbahar, V. Mansard, J. M. Mecca, M. Paul, T. Arrowood, T. M. Squires, Measuring interfacial polymerization kinetics using microfluidic interferometry. *J. Am. Chem. Soc.* **140**, 3173–3176 (2018).

25. Y. Suzuki, Y. Koyano, M. Nagaoka, Influence of monomer mixing ratio on membrane nanostructure in interfacial polycondensation: Application of hybrid mc/md reaction method with minimum bond convention. *J. Phys. Chem. B* **119**, 6776–6785 (2015).

26. T. D. Matthews, H. Yan, D. G. Cahill, O. Coronell, B. J. Mariñas, Growth dynamics of interfacially polymerized polyamide layers by diffuse reflectance spectroscopy and Rutherford backscattering spectrometry. *J. Membr. Sci.* **429**, 71–80 (2013).

27. B. Ukrainsky, G. Z. Ramon, Temperature measurement of the reaction zone during polyamide film formation by interfacial polymerization. *J. Membr. Sci.* **566**, 329–335 (2018).

28. X.-H. Ma, Z.-K. Yao, Z. Yang, H. Guo, Z.-L. Xu, C. Y. Tang, M. Elimelech, Nanofoaming of polyamide desalination membranes to tune permeability and selectivity. *Environ. Sci. Technol. Lett.* **5**, 123–130 (2018).

29. J. Xu, H. Yan, Y. Zhang, G. Pan, Y. Liu, The morphology of fully-aromatic polyamide separation layer and its relationship with separation performance of TFC membranes. *J. Membr. Sci.* **541**, 174–188 (2017).

30. A. Gierer, H. Meinhardt, A theory of biological pattern formation. *Kybernetik* **12**, 30–39 (1972).

31. Z. Tan, S. Chen, X. Peng, L. Zhang, C. Gao, Polyamide membranes with nanoscale Turing structures for water purification. *Science* **360**, 518–521 (2018).

32. V. Kolev, V. Freger, Hydration, porosity and water dynamics in the polyamide layer of reverse osmosis membranes: A molecular dynamics study. *Polymer* **55**, 1420–1426 (2014).

33. W. S. Price, O. Söderman, Self-diffusion coefficients of some hydrocarbons in water: Measurements and scaling relations. *J. Phys. Chem. A* **104**, 5892–5894 (2000).

34. R. F. Probstein, *Physicochemical Hydrodynamics: An Introduction* (John Wiley & Sons, 2005).

35. M. Dietzel, S. M. Troian, Formation of nanopillar arrays in ultrathin viscous films: The critical role of thermocapillary stresses. *Phys. Rev. Lett.* **103**, 074501 (2009).

36. J. Peng, H. Wang, B. Li, Y. Han, Pattern formation in a confined polymer film induced by a temperature gradient. *Polymer* **45**, 8013–8017 (2004).

37. E. Schäffer, S. Harkema, M. Roerdink, R. Blossey, U. Steiner, Morphological instability of a confined polymer film in a thermal gradient. *Macromolecules* **36**, 1645–1655 (2003).

38. L. E. Peng, Z. Yao, Z. Yang, H. Guo, C. Y. Tang, Dissecting the role of substrate on the morphology and separation properties of thin film composite polyamide membranes: Seeing is believing. *Environ. Sci. Technol.* **54**, 6978–6986 (2020).

39. K. S. Spiegler, O. Kedem, Thermodynamics of hyperfiltration (reverse osmosis): Criteria for efficient membranes. *Desalination* **1**, 311–326 (1966).

40. X. Wang, J. Li, H. D. Ha, J. Dahl, T. Head-Gordon, P. Alivisatos, AutoDetect-mNP: An unsupervised machine learning algorithm for automated analysis of transmission electron microscope images of metal nanoparticles. *JACS Au* **1**, 316–327 (2021).

41. R. Garcia, Nanomechanical mapping of soft materials with the atomic force microscope: Methods, theory and applications. *Chem. Soc. Rev.* **49**, 5850–5884 (2020).

42. J. M. Dennison, X. Xie, C. J. Murphy, D. G. Cahill, Density, elastic constants, and thermal conductivity of interfacially polymerized polyamide films for reverse osmosis membranes. *ACS Appl. Nano Mater.* **1**, 5008–5018 (2018).

43. Z. Wang, S. Liang, Y. Jin, L. Zhao, L. Hu, Controlling structure and properties of polyamide nanofilms by varying amines diffusivity in organic phase. *J. Membr. Sci.* **574**, 1–9 (2019).

44. D. Bhattacharya, S. Kole, O. Kizilkaya, J. Strzalka, P. P. Angelopoulou, G. Sakellariou, D. Cao, C. G. Arges, Electrolysis on a chip with tunable thin film nanostructured PGM electrocatalysts generated from self-assembled block copolymer templates. *Small* **17**, 2100437 (2021).

45. S. Shi, Y. Li, B.-N. Ngo-Dinh, J. Markmann, J. Weissmüller, Scaling behavior of stiffness and strength of hierarchical network nanomaterials. *Science* **371**, 1026–1033 (2021).

46. N. E. Persson, P.-H. Chu, M. McBride, M. Grover, E. Reichmanis, Nucleation, growth, and alignment of poly (3-hexylthiophene) nanofibers for high-performance OFETs. *Acc. Chem. Res.* **50**, 932–942 (2017).

47. S. Shin, F. Menk, Y. Kim, J. Lim, K. Char, R. Zentel, T.-L. Choi, Living light-induced crystallization-driven self-assembly for rapid preparation of semiconducting nanofibers. *J. Am. Chem. Soc.* **140**, 6088–6094 (2018).

48. J. Gigault, H. El Hadri, B. Nguyen, B. Grassl, L. Rowenczyk, N. Tufenkji, S. Feng, M. Wiesner, Nanoplastics are neither microplastics nor engineered nanoparticles. *Nat. Nanotechnol.* **16**, 501–507 (2021).

49. B. H. Kim, J. Heo, S. Kim, C. F. Reboul, H. Chun, D. Kang, H. Bae, H. Hyun, J. Lim, H. Lee, Critical differences in 3D atomic structure of individual ligand-protected nanocrystals in solution. *Science* **368**, 60–67 (2020).

50. H. An, J. W. Smith, W. Chen, Z. Ou, Q. Chen, Charting the quantitative relationship between two-dimensional morphology parameters of polyamide membranes and synthesis conditions. *Mol. Syst. Des. Eng.* **5**, 102–109 (2020).

51. J. R. Kremer, D. N. Mastronarde, J. R. McIntosh, Computer visualization of three-dimensional image data using IMOD. *J. Struct. Biol.* **116**, 71–76 (1996).

52. Q. Chen, J. M. Smith, J. Park, K. Kim, D. Ho, H. I. Rasool, A. Zettl, A. P. Alivisatos, 3D motion of DNA-Au nanoconjugates in graphene liquid cell electron microscopy. *Nano Lett.* **13**, 4556–4561 (2013).

53. J. Schindelin, I. Arganda-Carreras, E. Frise, V. Kaynig, M. Longair, T. Pietzsch, S. Preibisch, C. Rueden, S. Saalfeld, B. Schmid, J.-Y. Tinevez, D. J. White, V. Hartenstein, K. Eliceiri, P. Tomancak, A. Cardona, Fiji: An open-source platform for biological-image analysis. *Nat. Methods* **9**, 676–682 (2012).

54. D. Stalling, M. Westerhoff, H.-C. Hege, Amira: A highly interactive system for visual data analysis. *Visualization Handbook* **38**, 749–767 (2005).

55. D. Legland, I. Arganda-Carreras, P. Andrey, MorphoLibJ: Integrated library and plugins for mathematical morphology with ImageJ. *Bioinformatics* **32**, 3532–3534 (2016).

56. R. Dougherty, K.-H. Kunzelmann, Computing local thickness of 3D structures with ImageJ. *Microsc. Microanal.* **13**, 1678–1679 (2007).

57. S. Nembrini, I. R. König, M. N. Wright, The revival of the Gini importance? *Bioinformatics* **34**, 3711–3718 (2018).

58. G. J. McLachlan, K. E. Basford, *Mixture Models: Inference and Applications to Clustering* (Dekker, 1989), vol. 38.

59. Q. Ouyang, R. Li, G. Li, H. L. Swinney, Dependence of Turing pattern wavelength on diffusion rate. *J. Chem. Phys.* **102**, 2551–2555 (1995).

60. B. Giner, A. Villares, S. Martín, H. Artigas, C. Lafuente, Study of the temperature dependence of surface tensions of some alkanol+ hexane mixtures. *J. Chem. Eng. Data* **52**, 1904–1907 (2007).

61. T. M. Aminabhavi, V. B. Patil, M. I. Aralaguppi, H. T. S. Phayde, Density, viscosity, and refractive index of the binary mixtures of cyclohexane with hexane, heptane, octane, nonane, and decane at (298.15, 303.15, and 308.15) K. *J. Chem. Eng. Data* **41**, 521–525 (1996).

62. E. K. Dimitriadis, F. Horkay, J. Maresca, B. Kachar, R. S. Chadwick, Determination of elastic moduli of thin layers of soft material using the atomic force microscope. *Biophys. J.* **82**, 2798–2810 (2002).